AIAA SciTech Forum
January 3-7, 2022, San Diego, CA & Virtual
AIAA SCITECH 2022 Forum

10.2514/6.2022-1020

Tonal noise measurements of a small propeller in an open and closed test facility

E. van Bokhorst[1] and H. Brouwer[2]
Netherlands Aerospace Centre NLR, 1006 BM Amsterdam, The Netherlands

In this paper experiments and simulations on tonal noise of a small propeller are described. Experiments were carried out in the open-jet and closed test section configuration of the Aeroacoustic Wind Tunnel at NLR Marknesse. From previous investigations it has been found that when acoustic beamforming techniques are applied, the acoustic source is not located at the propeller blade itself. Therefore a new propeller steering function for acoustic beamforming is introduced which incorporates the operating conditions of the propeller. With the new steering function it is more easy to identify the source location however the large depth of field prevents the possibility to use three dimensional beamforming. Instead, to define the y-coordinate of the virtual source location the open-jet simulations are used. The final comparison between the open-jet and closed test section measurements shows that the resonances in the tunnel and reflections influence the sound pressure levels significantly. More work is needed to fully understand these effects.

Nomenclature

A	=	auto-power
α	=	axial wavenumber
B	=	blade number
g	=	steering function
n	=	harmonic number
H	=	half height of the wind tunnel
C_p	=	pressure coefficient
M_t	=	tip Mach number
M_x	=	streamwise Mach number
r	=	radial coordinate
$S(\varphi)$	=	amplitude function
θ	=	pressure coefficient
ξ_n	=	coordinates of n-th gridpoint
p	=	acoustic pressure
W	=	half width of the wind tunnel
x	=	axial coordinate
x_n	=	coordinates of n-th microphone
φ	=	polar angle in $(x/\beta, r)$ plane
Ω	=	angular velocity
ω	=	angular frequency

[1] R&D engineer, Department of Vertical flight and Aeroacoustics.
[2] Senior Scientist, Department of Vertical flight and Aeroacoustics.

I. Introduction

Propellers or turboprops remain the most efficient propulsion system for medium speed aircraft and hold great potential for electric propulsion for the coming decades. Even though propellers are great for propulsion the disadvantage is the amount of noise they generate. Aerodynamic noise from propellers can be divided in different categories such as rotational noise, vortex noise and noise caused by interaction and distortion [1]. In the current investigation the focus in the simulation and experiments will be on the rotational, tonal noise. Rotational noise is caused by the pressure distribution on the blades. At a stationary observer this pressure is an oscillating pressure, sound, which frequency is determined by the number of blades and rotational speed of the propeller and the magnitude by the thrust and torque distribution on the blades, and the thickness of the blades.

When low-noise propeller blades are designed, acoustic measurements have to be carried out to verify the design. Due to the application it is preferred to carry out this test at Mach numbers up to 0.6-0.7 which are usually done in wind tunnels with a closed test section. Carrying out such measurements brings a number of challenges:

1) The propeller is placed in a reverberant environment. Due to reflections measurements with single wall-mounted microphones will not be representative and an array of microphones needs to be used. With an array of microphones the source can be located and quantified using acoustic beamforming. For coherent noise sources such as tonal noise the beamform source maps will still be contaminated by the reflections. With conventional beamforming the noise source is represented by a monopole in the free-field as described by the appropriate Green's function. Sureshkumar et al. (2019) adapted the Green's function to represent a noise source in a closed test section, and applied it to an open rotor. They found that tonal noise measurements will still be contaminated by reflections even when the wind tunnel walls are acoustically treated [2]. Another approach was applied by filtering of the cross-correlation matrix to mitigate the effects of reflections [3]. The approach was successful for broadband noise where it was possibly to separate the reflections from the actual source. For harmonic sources the method could not be applied.
2) The dimensions of the test section of most high-speed wind tunnels lead to the fact that the microphone array is placed in the near field of the propeller which can lead to issues when the usual far-field assumptions are used as for example in the steering function for acoustic beamforming. When acoustic beamforming on a propeller sound source is applied the source does not appear at the same location as the propeller [4]. Due to this the propeller source can be wrongly determined and/or quantified.

The goal of the current investigation is to gain a better understanding of the problems described above. Therefore experiments and acoustic simulations were carried out on the same propeller both in an open-jet and closed wind tunnel facility. The tested propeller is an 11x6 APC propeller with 4 blades shown in Figure 1. Even though for a propeller of this size open-jet measurements would suffice, the idea is to mimic the same conditions and corresponding problems as would occur for an industrial propeller tested at realistic Mach and Reynolds numbers.

Figure 1: APC propeller used for the experiments and simulations.

II.Simulation tools

Acoustic simulations were carried out both in an open-jet and closed test section configuration. For both cases the flow field induced by a propeller is computed with MAEPROP, NLR's lifting-line method [5]. For the open-jet the solution of the acoustic tonal field generated by NLR's rotating lifting-line acoustics method, ROLLAC is used.

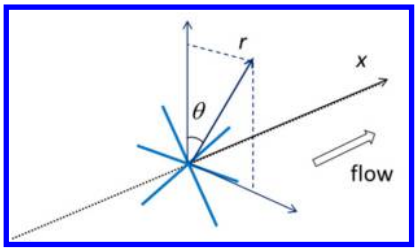

Figure 2: Coordinate system used in the simulation.

The rotating lifting-line source in a uniform flow in x-direction, shown in Figure 2 is:

$$\left[\nabla^2 - \left(\frac{\mathrm{D}}{\mathrm{D}t}\right)^2\right] p = -\nabla \cdot \frac{1}{r}\left[\vec{L}(r) - \overline{\overline{D}}(r) \cdot \nabla\right] \delta(x) \sum_{j=0}^{B-1} \delta\left(\theta - \Omega t - \frac{2\pi j}{B}\right) \tag{1}$$

with $\frac{\mathrm{D}}{\mathrm{D}t} = \frac{\partial}{\partial t} + M\frac{\partial}{\partial x}$. Here $\vec{L}$ is the force on the blade per unit span, i.e. lift and drag, and $\overline{\overline{D}}$ is a tensor with elements that are proportional to either the pitching moment, also per unit span, or the area of the local cross section of the blade. The latter is responsible for the so-called thickness noise. B is the number of blades and Ω the rotational speed. Ω is positive if the rotor rotates in clockwise direction viewed from an upstream position. Variables are made dimensionless on the tip radius, the ambient density, and the speed of sound.

The pressure p can be written as a sum of harmonics of the Blade Passing Frequency (BPF) denoted by $\hat{p}_n$. , In the open-jet is the solution for $\hat{p}_n$ is derived in cylindrical coordinates:

$$\begin{aligned}\hat{p}_n(x, r_p) = \frac{B}{8\pi} e^{inB\theta} \int_{-\infty}^{\infty} e^{i\alpha x} H_{nB}^{(2)}(\gamma r_p) \int_{r_h}^{1} J_{nB}(\gamma\rho) \left\{ \alpha L_x + \frac{nB}{\rho} L_\theta \right. \\ \left. - i\left[\alpha^2 D_{xx} + \alpha\frac{nB}{\rho}(D_{x\theta} + D_{\theta x}) + \left(\frac{nB}{\rho}\right)^2 D_{\theta\theta}\right]\right\} \mathrm{d}\rho\mathrm{d}\alpha \\ \stackrel{\text{def}}{=} \frac{i}{4} e^{inB\theta} \int_{-\infty}^{\infty} e^{i\alpha x} H_{nB}^{(2)}(\gamma r_p) \int_{r_h}^{1} J_{nB}(\gamma\rho) Q_n(\alpha, \rho) \mathrm{d}\rho\mathrm{d}\alpha\end{aligned} \tag{2}$$

Where α is the axial wavenumber $H_n^{(2)}$ and J_n the Hankel and Bessel functions, γ the radial wavenumber ($\gamma^2 = (\omega + M\alpha)^2 - \alpha^2$), r_h the radius of the hub, L_x,L_θ the forces on the blade and D_{xx},$D_{x\theta}$, $D_{\theta x}$ and $D_{\theta\theta}$ components which are proportional to thickness or pitching moment.

For the closed test section with a width $2W$ and height $2H$ the sound source, Q, is again the rotating lifting-line source described by Eq. 1. With the no-flow boundary conditions on the wall the following solution for $\hat{p}_n$ can be found by using the Green's function derived in Ref. [2]:

$$\hat{p}_n(x,y,z) = \frac{i}{2WH}\sum_{j=0}^{\infty}\sum_{m=0}^{\infty} e^{i\alpha_{jm}^{\pm}x}\frac{\psi_j\left(\frac{y}{W}\right)\psi_m\left(\frac{z}{H}\right)}{w_j w_m\sqrt{\omega^2-\beta^2\gamma_{jm}^2}}\int_{r_h}^{1} Q_n(\alpha_{jm}^{\pm},\rho)\int_0^{2\pi}\psi_j\left(\frac{\eta}{W}\right)\psi_m\left(\frac{\zeta}{H}\right)e^{inB\varphi}\mathrm{d}\varphi\mathrm{d}\rho \quad (3)$$

with $w_j = 2$ for $j = 0$, and $w_j = 1$ for $j \neq 0$. Further $\psi_j(\xi) = \cos\left(\frac{j\pi}{2}(\xi+1)\right)$, $\gamma_{jm}^2 = \left(\frac{j\pi}{2W}\right)^2 + \left(\frac{m\pi}{2H}\right)^2$ and $\alpha_{jm}^{\pm} = \frac{1}{\beta^2}\left[\omega M \pm \sqrt{\omega^2-\beta^2\gamma_{j,m}^2}\right]$. η and ζ are the cartesian coordinates in the (φ, ρ) system.
For $x = 0$ the solution is singular and the series does not converge. It can be shown that to reach a specified accuracy the total number of modes to be included is proportional to $1/x^2$.

For both methods the blade geometry from the experimental propeller has been used. For this purpose the blades were scanned with a 3D scanner (GOM ATOS Core 200) with a resolution of 0.012mm. In Figure 3 the 3D scanned surface is shown.

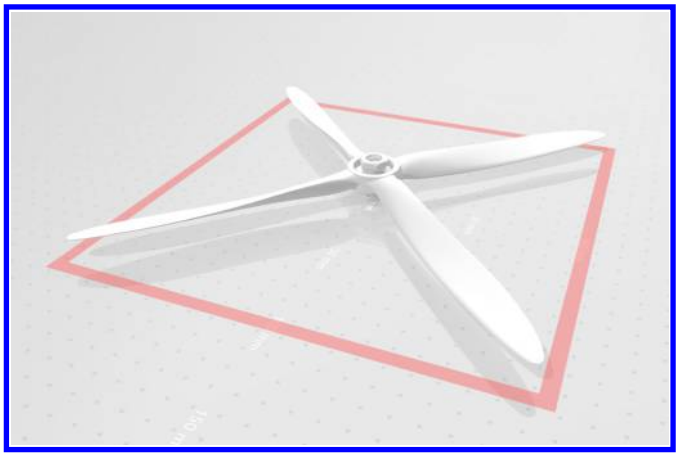

Figure 3: 3D scanned propeller blades.

III.Experimental set-up

Experiments were carried out in the aeroacoustic windtunnel (AWT) at NLR Marknesse. The nozzle exit is 0.95mx0.95m which is also the size of the closed test section. The propeller was driven by a 850Kv rated electric motor (A50-8S Turnado V4 kv850) and controlled by an electronic speed controller (Trampaboards vesc-6-mkv). No external cooling was applied which did not cause any issues in the current experiment. However, in future experiments an active cooling system would be applied to be able to run the propeller for a longer time at high RPM's. In Figure 4 the lay-out of both set-ups are shown.

For the open-jet a 64 channel microphone array (PCB 378A06) is used. For the closed test section a 96 channel array (M51) is used. Measurements were carried out for 30 seconds with a sampling frequency of 40.96kHz. On one of the channels a 1P-signal was recorded which was generated by a small laser detecting a marker on the back of the motor. With the 1P-signal the measurements could be phase-averaged in post-processing.

The main variable in test was the RPM which ranged from 6000 to 10000 with wind tunnel velocities of 10 and 20m/s. This leads to an advance ratio range from 0.21 to 0.54 where the advance ratio was defined as $J = U_\infty/(D_{prop}\frac{\Omega}{2\pi})$ and a tip Mach number range from 0.26 to 0.43.

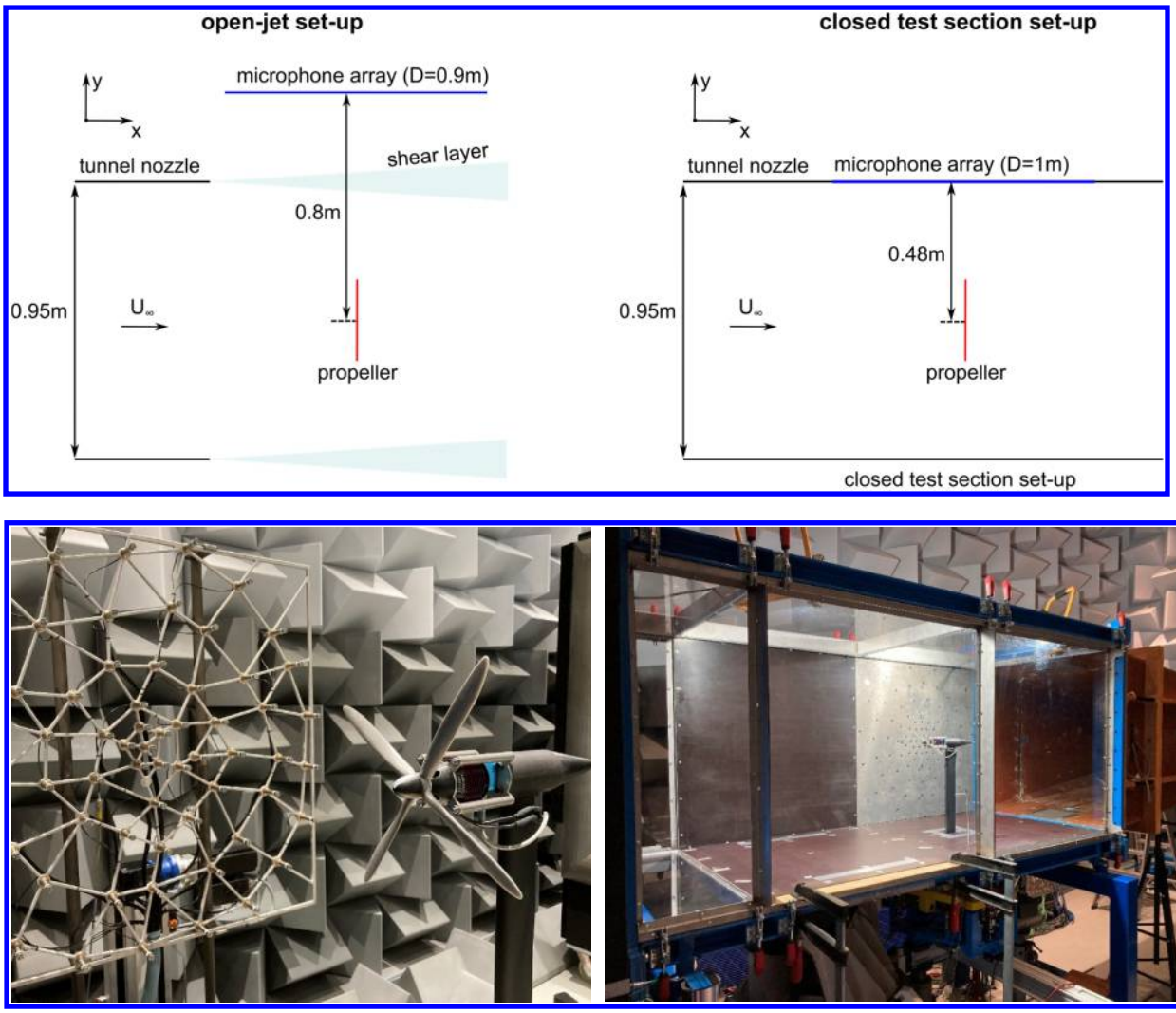

Figure 4: Experimental-set up in the open-jet and closed test section.

IV.Beamforming on a propeller sound source

With conventional beamforming the source auto-powers, A, are obtained with:

$$A = \frac{\boldsymbol{g}^* \boldsymbol{C} \boldsymbol{g}}{\|\boldsymbol{g}\|^4} \tag{4}$$

where $\boldsymbol{C}$ is the cross-power matrix, and $\boldsymbol{g}$ the steering function. The sound source is described as a monopole in a uniform flow in which case the steering function writes:

$$g_{mono} = \frac{-e^{2\pi i f \Delta t_e(x_n,\xi_n)}}{4\pi\sqrt{(M \cdot (x_n - \xi_n)^2 + \beta^2 \|\boldsymbol{x}_n - \boldsymbol{\xi}_n\|}} = \frac{-e^{2\pi i f \Delta t_e(x_n,\xi_n)}}{4\pi R} \tag{5}$$

where f is the frequency, $\Delta t_e(\boldsymbol{x}_n, \boldsymbol{\xi}_n)$ the time delay for microphone $\boldsymbol{x}_n$ and grid point $\boldsymbol{\xi}_n$, M the Mach number and $\beta = (1 - M^2)$.

In Figure 5**Error! Reference source not found.** the maximum SPL value in *xz*-planes at varying y is determined for the open-jet simulation. The source level decreases the closer the grid is placed to the array (at y=0.8m), which is directly due to the 1/R term in the steering function. This becomes clear when the decay factor is set to 1 as is also shown in Figure 3, where now the maximum source level is found between y=-0.3m and y=0.3m. The dependency of source location and level on the chosen steering function is described in detail in reference [6]. Since for the propeller noise source the exact source location is not known beforehand it is chosen to first set the decay term to 1 to find the virtual source location, after that the decay term is set to 1/R to find the actual source level.

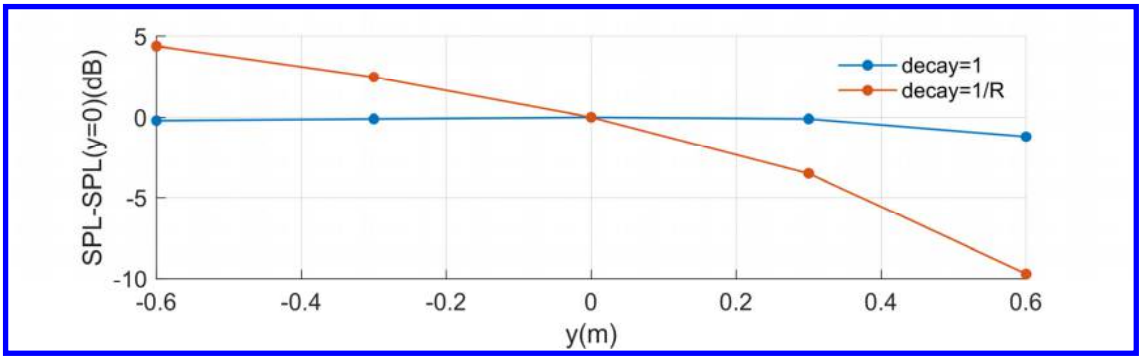

Figure 5: Difference between maximum SPL value found in the xz-plane placed at location y and the maximum SPL value found at y=0.

Next the dependency of the virtual source location on the propeller operating condition was studied theresults of which are shown in Figure 6 where the coordinates of the virtual source are plotted. The lower the RPM the further away the virtual source location lies from the propeller.

This follows directly when the sound waves impinging on the array are considered as shown in Figure 6 as also shown in reference [4]. The location of the virtual source location can also be estimated from the Mach radius which is defined as the radius where in theory the tip Mach number will be 1 [7], which consequently for a subsonic propeller will lie outside the propeller disk. The Mach radius is determined with:

$$r^* = \frac{1 - M_x cos\theta}{M_t \sin\theta} \tag{6}$$

Where r^* is the Mach radius normalized with the propeller radius, θ is the angle between the microphone and the streamwise direction x. When θ=90° is considered which is the location of the middle of the array Eq. 6 simplifies to $r^* = 1/M_t$. In Figure 6 the Mach radius is shown with the broken lines for both the lowest and highest RPM. For the high RPM the Mach radius coincides with the expected value while for the low RPM the virtual source location is located at a larger r then expected. For the low RPM and frequencies the array is still in the near field of the source which could therefore explain this discrepancy.

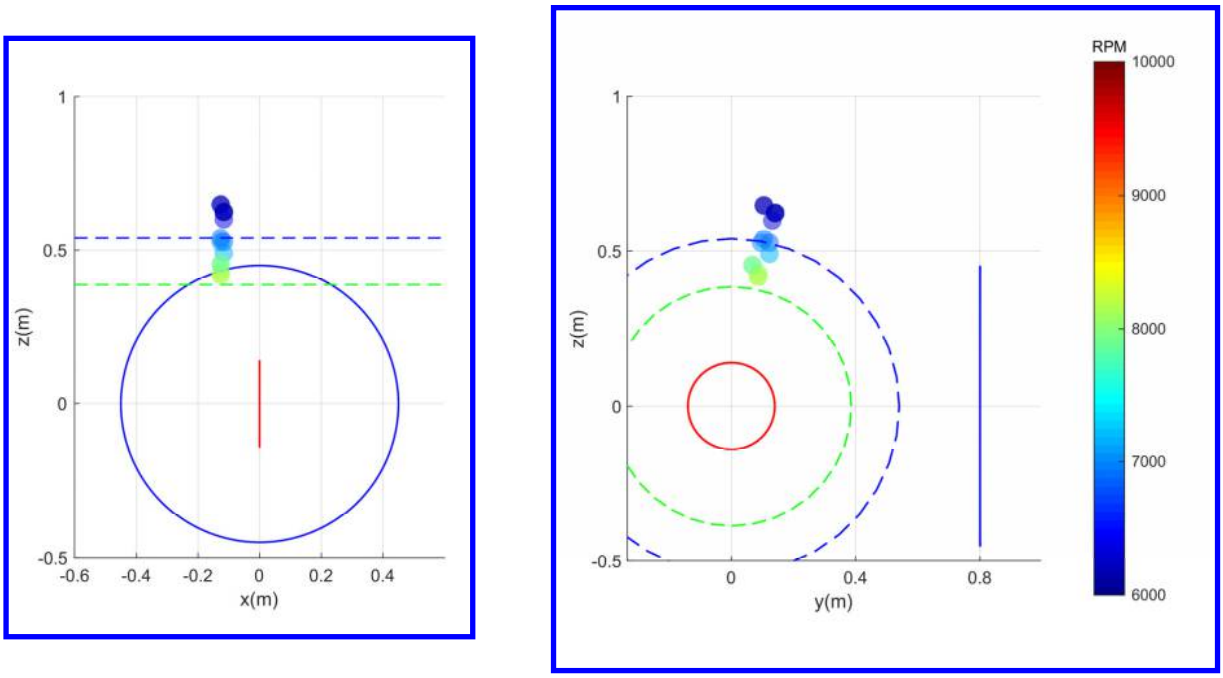

Figure 6: Virtual source location obtained with conventional beamforming as a function of RPM. In red the propeller is shown and in blue the array. The broken lines show the Mach radius for the highest (green) and lowest (blue) RPM.

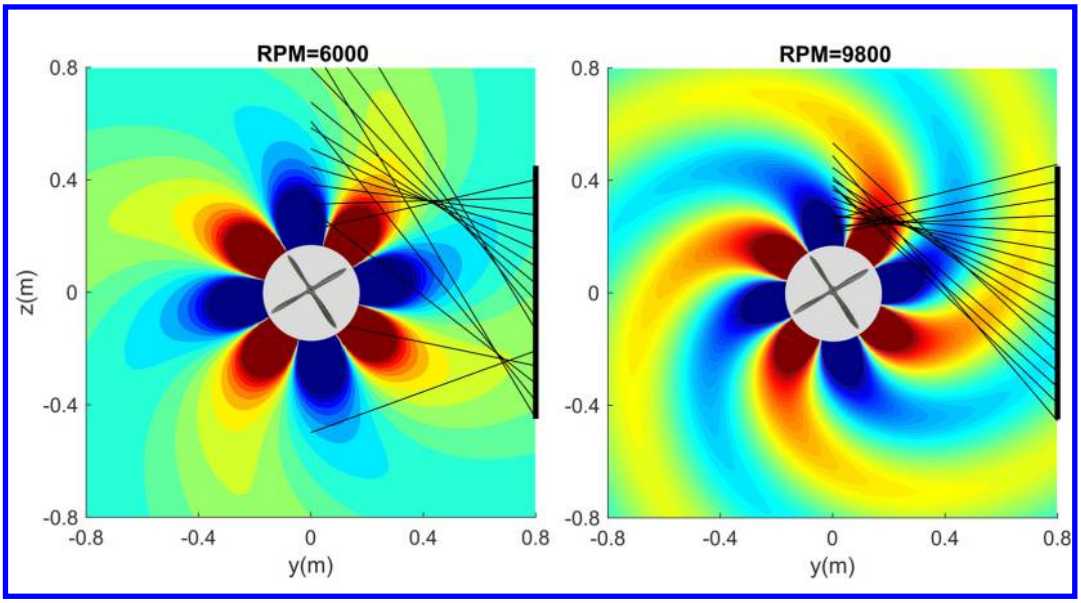

Figure 7: Distribution of the real part of the acoustic pressure. At y=0.8m the array is drawn, the black lines coming from the array are perpendicular to the wavefronts impinging on the array.

From the analysis with conventional beamforming it is found that the virtual source location moves when describing the propeller sound source as a monopole. While for the current case with a single dominant source this might not be a problem for cases with more than one source, as for example in a reverberant environment, it might be more difficult to locate the correct source.

Therefore here a propeller steering function is introduced. For the case where $R \gg R_{tip}$, in the far-field, the solution of Equation 1 simplifies to:

$$p_n(x, r, \theta, t) \sim S(\varphi) \frac{1}{R} e^{i(\alpha_0 x - \gamma_0 r + nB(\theta - \Omega t))} \tag{7}$$

where $S(\varphi)$ is the amplitude function which contains the blade loading and thickness noise terms and

$$\alpha_0 = \frac{-nB}{\beta^2}(M - cos\varphi) \tag{8}$$

$$\gamma_0 = \frac{-nB\, sin\, \varphi}{\beta} \tag{9}$$

Here r is the distance to the propeller axis and $x = \beta R\cos\varphi$, $r = R\sin\varphi$. To find the amplitude function $S(\phi)$ with Equation 2 the following propeller steering function is defined:

$$g_{prop}(x, r, \theta, \omega) = \frac{1}{R} e^{i(\alpha_0 x - \gamma_0 r + nB\theta)} \delta(-\Omega nB - \omega) \tag{10}$$

Since the operating conditions of the propeller are now included the virtual source location is now almost constant (Figure 8). Because the array is, especially for low RPM, still in the near field there is still a small dependency on RPM.

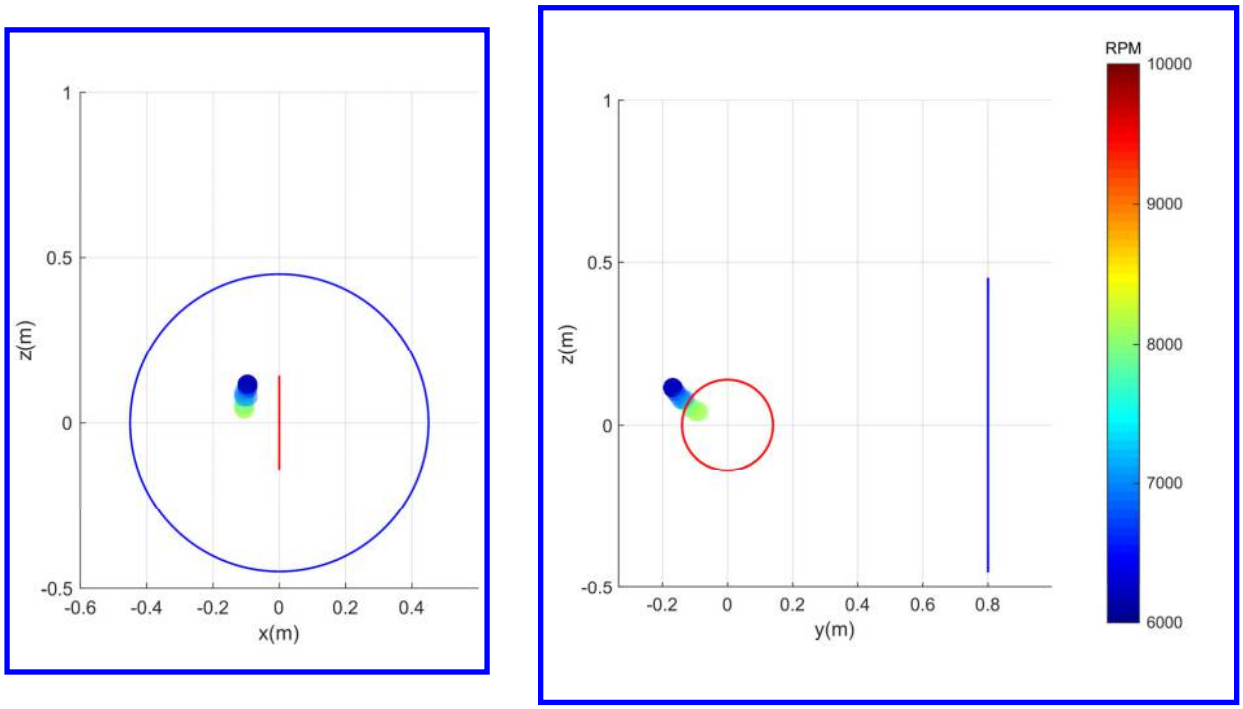

Figure 8: Virtual source location obtained with propeller steering function as a function of RPM. In red the propeller is shown and in blue the array.

V. Results and discussion

A. Open-jet

In Figure 9 the auto-spectra of the background measurement and unloaded (without propeller) and loaded motor cases are shown. As for the unloaded motor case several peaks appear. At the shaft frequency corresponding to the rotations per second (RPS) a peak is shown as well at the harmonics of this peak with a dominating peak at 5 times the rotational speed (5/4BPF). The same peaks are present when the motor is loaded with the propeller with 4 blades. The shaft frequencies indicate that the blade was not properly balanced. The high level at 5 times the rotational speed might be a resonance of the system since in the unloaded case it is significantly higher than the lower harmonics of the rotational speed.

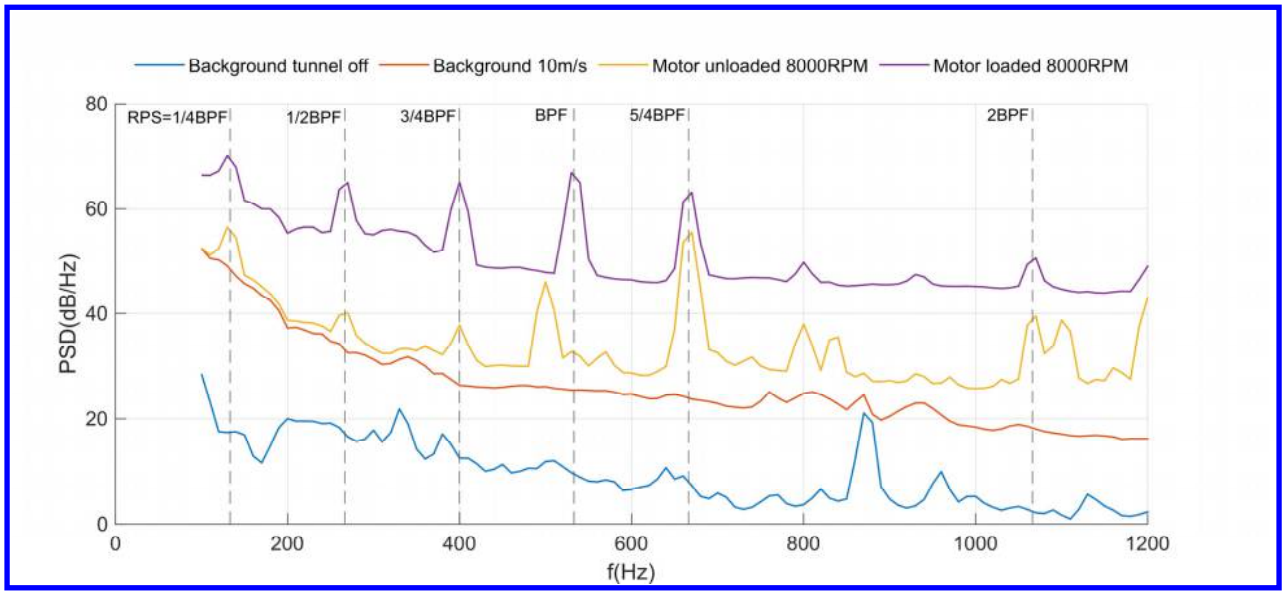

Figure 9: Auto-spectra of background measurements and measurements with a loaded and unloaded motor.

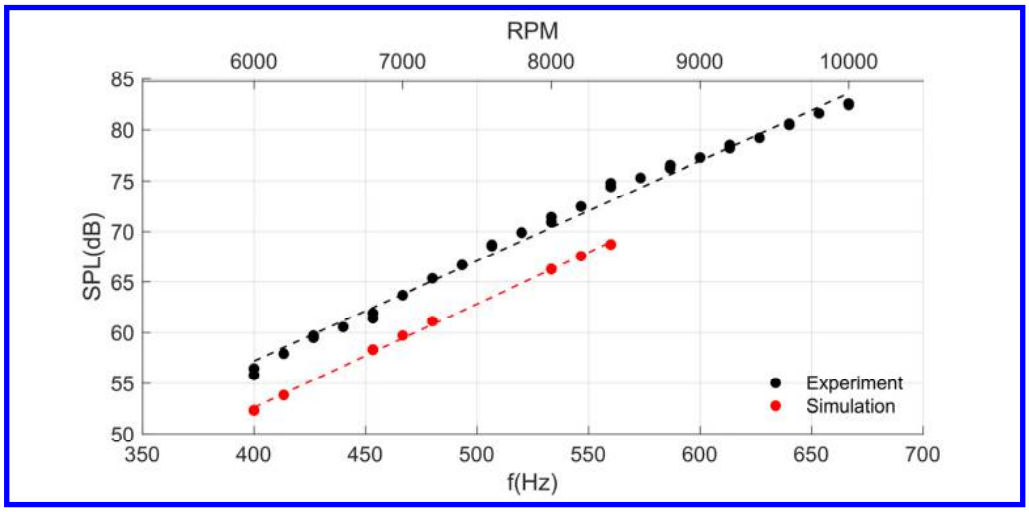

Figure 10: SPL values obtained from the mean of all microphones.

Next the source levels of the 1st BPF are compared between the simulation and experiment by taking the mean SPL measured at the array (Figure 10). Since the simulation tool was created for industrial propellers and operating conditions it did not converge for each experimental condition. There seems to be a bias error between the experiment and simulation while the trend for both cases is very similar. At the moment it is investigated if the bias error is caused by the experiment or simulation.

The virtual source location obtained with conventional beamforming is shown in Figure 11. Compared to the simulation, shown with stars, the source is further from the propeller than expected for the lower RPM while for the high RPM it is at a similar location. The y-location varies significantly which was not observed in the simulation. The depth-of-field defined as the distance where the response of an out-of-plane source is noticed [7], is a function of frequency and array aperture. Where for the lower frequency the depth-of-field becomes larger which makes it more difficult to define the location of the maximum. The same principle holds for the simulation however the absence of small experimental errors allows to determine the location of the maximum SPL with high accuracy and hence the variation in y-location is not observed there.

The variation in y-location is clearly shown in the source levels obtained with conventional beamforming at the virtual source location (Figure 12). This makes the 3D beamforming technique not suitable for the current measurements where frequencies are low and the array is in the near-field of the array. Other techniques such as tomographic beamforming should be used to define the virtual source location with higher accuracy [7].

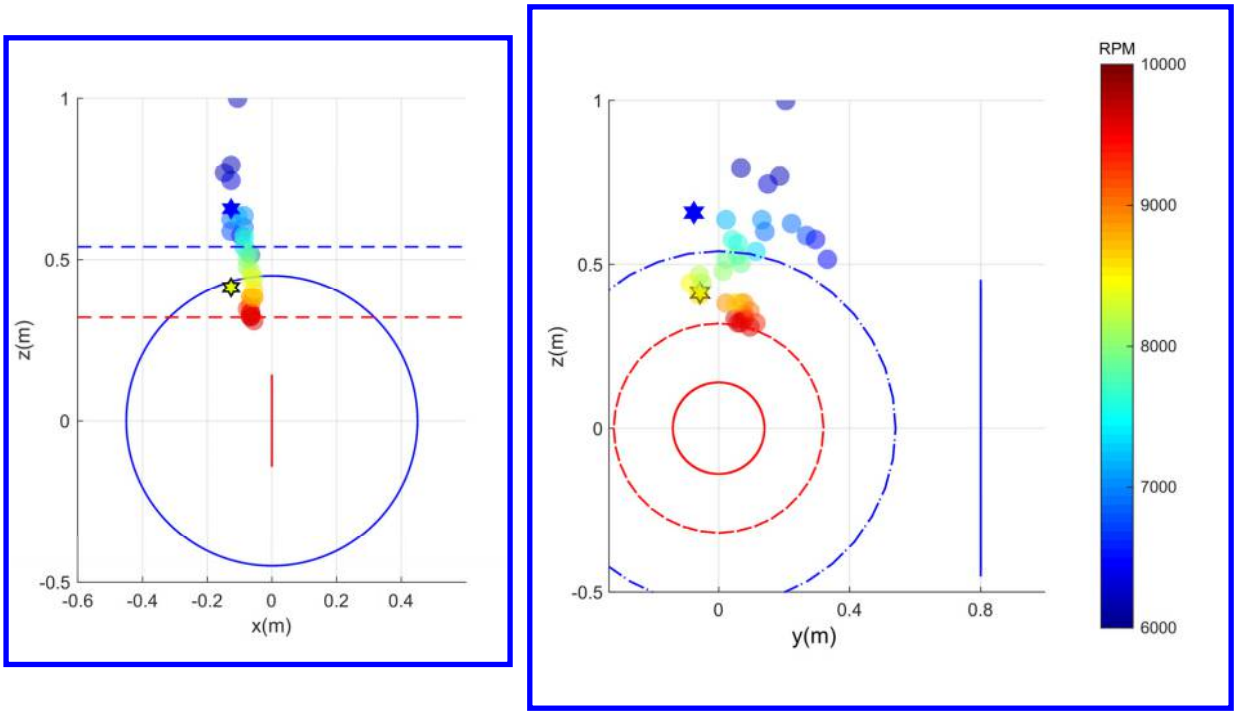

Figure 11: Virtual source location obtained with conventional beamforming as a function of RPM. In red the propeller is shown and in blue the array. The broken lines show the Mach radius for the highest (red) and lowest (blue) RPM. The stars indicate the virtual source location from the simulation where blue and green represent the lowest and highest RPM for the simulation respectively.

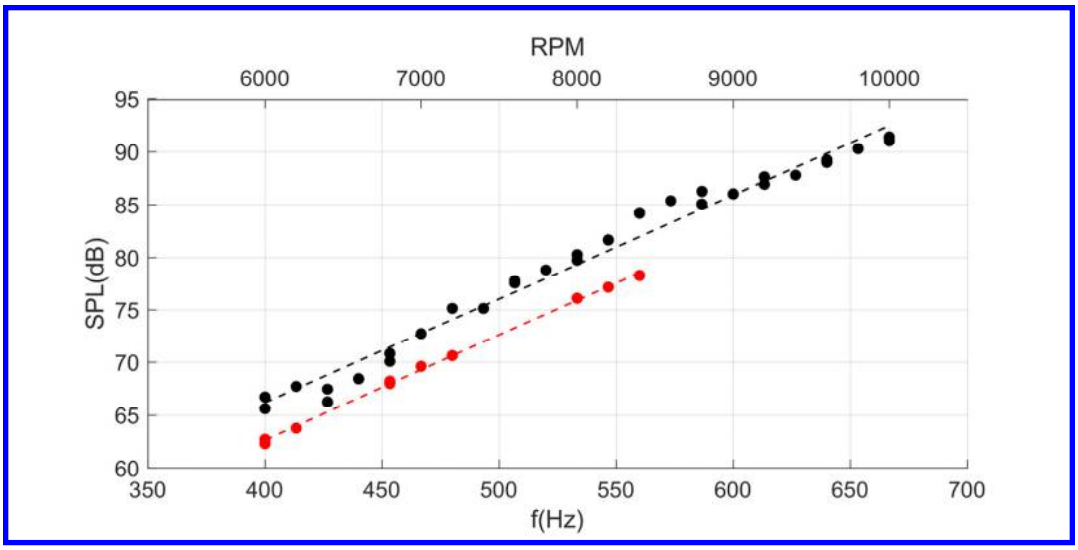

Figure 12: SPL values at the virtual source location obtained with conventional beamforming.

Next the propeller steering function is applied to the open-jet measurements. In Figure 13 the virtual source location is shown. The virtual source location has moved closer to the propeller. The variation in depth (y-coordinate) is still present however less as for the monopole steering function case. This was expected since the depth of field is a function of the set-up parameters and not solely the source representation. To reduce the effect of depth of field on the source level, the maximum SPL was determined in the *xz*-plane where the virtual source location in the simulation was found. In Figure 14 the source levels obtained with this method is compared to the simulation values.

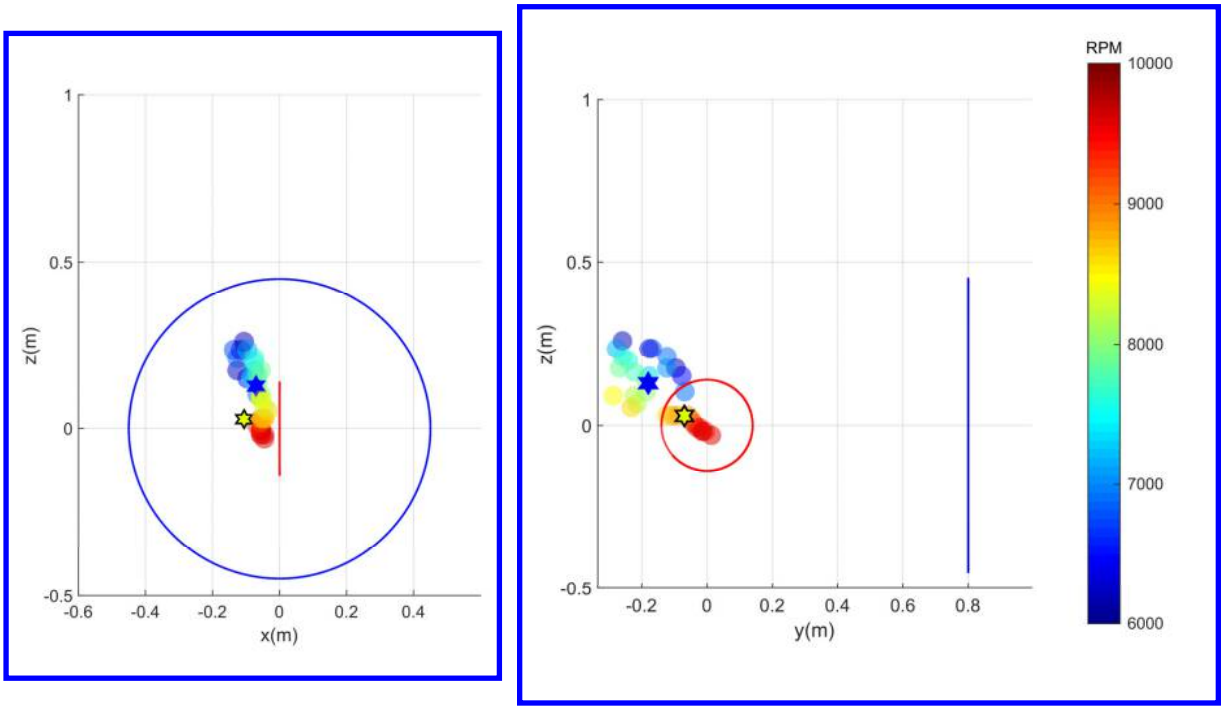

Figure 13: Virtual source location obtained with propeller steering function as a function of RPM. In red the propeller is shown and in blue the array. The dotted lines show the Mach radius for the highest (red) and lowest (blue) RPM. The stars indicate the virtual source location from the simulation where blue and green represent the lowest and highest for the simulation respectively.

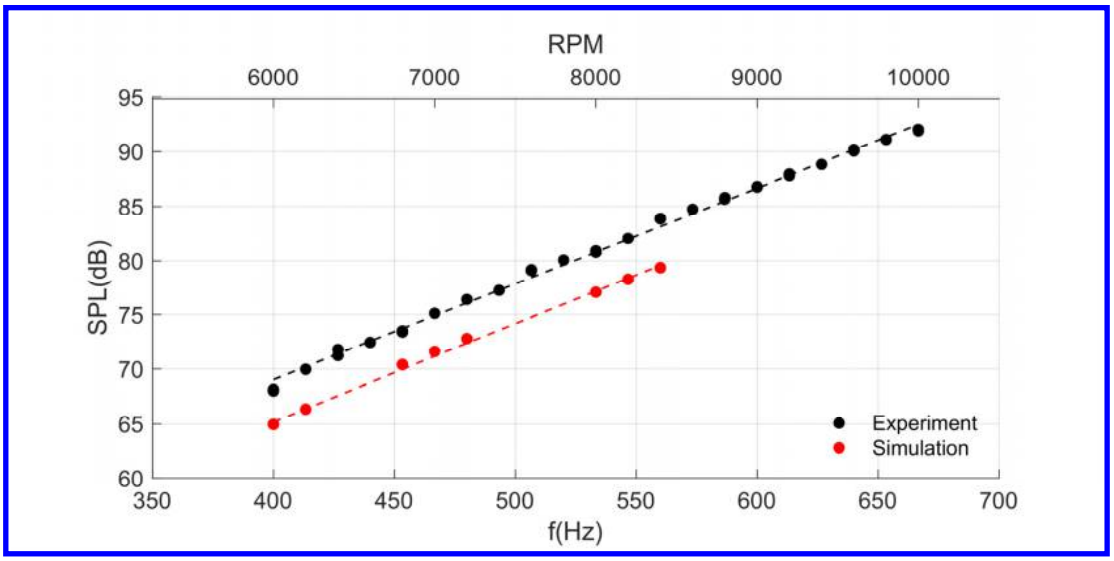

Figure 14: SPL values at the virtual source location obtained with the propeller steering function for the open-jet. For the experimental data the virtual source location is found in the xz-plane where the virtual source location in the simulation was found.

From the open-jet measurements it has been found that the propeller steering function can be applied to locate the propeller source. While for the current experiment there was only one dominating source and the technique did not add a lot of new information compared to taking for example just the mean SPL at all microphones. It is imagined that for cases where are there are more than source, for example several propellers, this specific steering function can be useful to separate the different sources.

B. Closed test section

In Figure 15 the Campbell diagram is shown for the closed test section measurements. Just as in the open-jet measurements the levels for the 5RPS are strong. At the frequencies for 2nd and 3rd BPF background noise is dominating the measurements. This was also shown when the signal-to-noise ratio was determined, defined as the difference between the sound pressure level with and without phase-locked averaging. In the remainder of this section again the focus is on the 1st BPF.

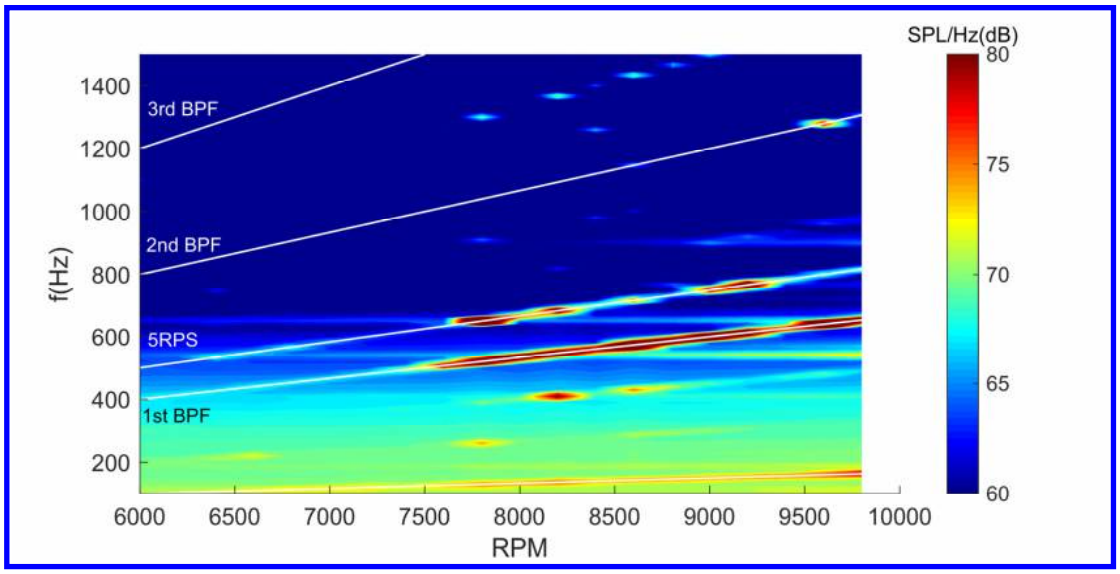

Figure 15: Campbell diagram for closed test-section measurements.

In Figure 16 the source maps obtained with conventional beamforming for the open-jet and closed test section measurements are compared. For the open-jet measurements the source maps are clean and the source moves towards the propeller with RPM. For the closed test section measurements the source maps are contaminated by image sources caused by the reflections.

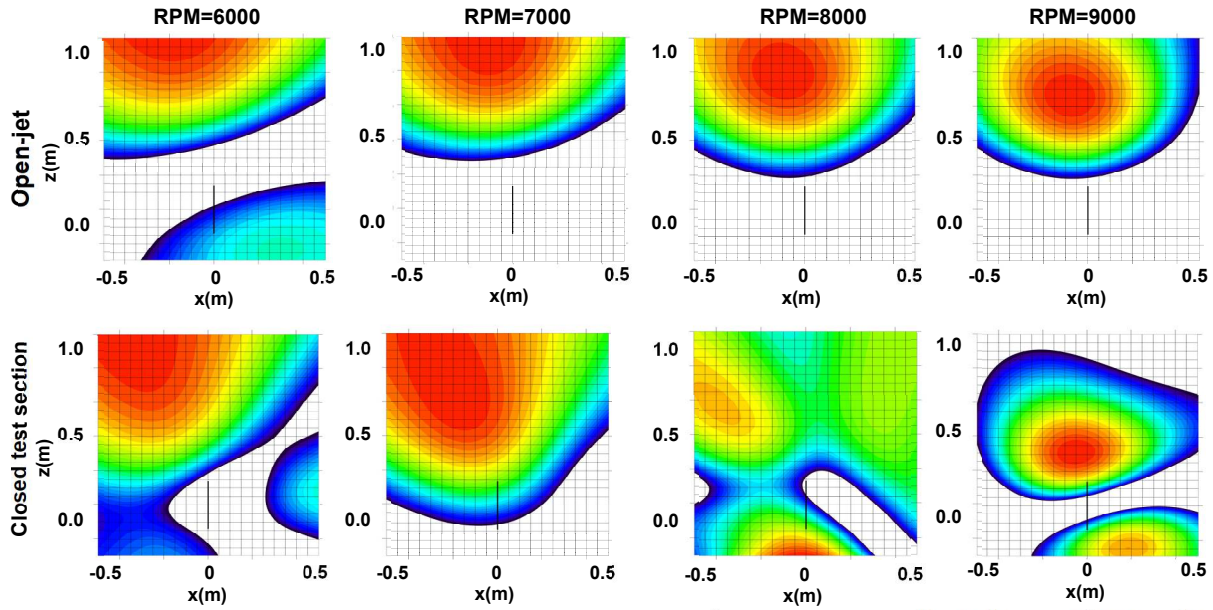

Figure 16: Source maps for different RPM. On the first row the measurements from the open-jet are shown on the second row the measurements for the closed test section.

In
Figure 17 the source maps for the closed test section measurements are shown when the propeller steering function is applied. For all cases it is now more clear which source corresponds to the propeller source such that the source level can be correctly determined. It is shown that there are still other sources present in the source maps since the image sources of the propeller source are still present.

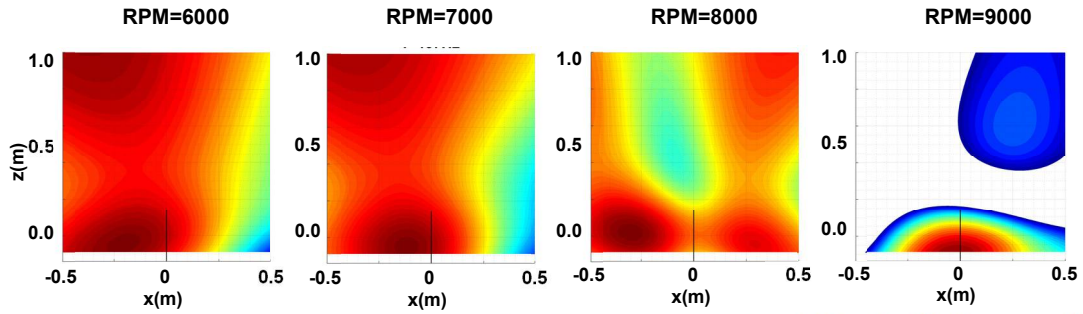

Figure 17: Source maps for the closed test section measurements obtained with the propeller steering function.

The y-coordinate of the virtual source location both varies for the simulation and experiment (Figure 18) where the grid extends up to y=-0.475. The reflections seem to deteriorate the depth of field since for both the experiment and simulation the y-coordinate varies while for the open-jet this was not the case for the simulations.

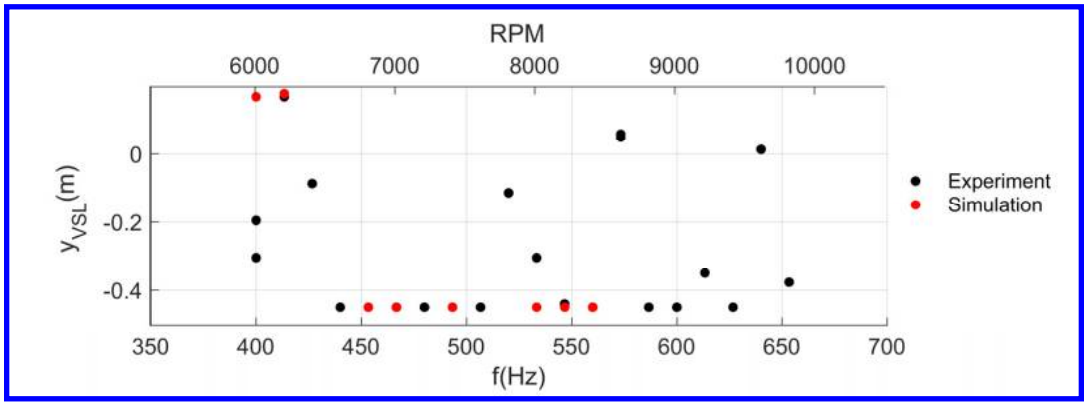

Figure 18: y-coordinate of the virtual source location for the closed test section configuration.

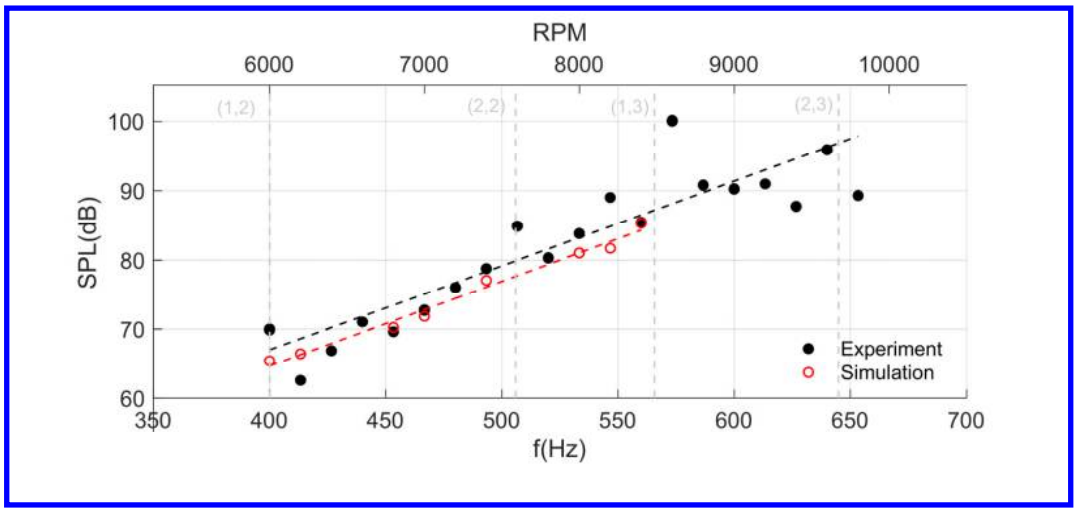

Figure 19: SPL values at the virtual source location obtained with the propeller steering function for the closed test-section. The SPL value is found in the xz-plane where the virtual source location in the open-jet simulation was found.

In Figure 19 the source levels from the simulation are compared to the experiment by again using the xz-plane where the virtual source is found in the open-jet simulation. The levels and trends are similar, however for the experiment there are several outliers. Some of the outliers line up with the resonance frequencies of the wind tunnel test section determined with:

$$\omega_{j,m} = \sqrt{\beta^2 \left(\left(\frac{j\pi}{2W} \right)^2 + \left(\frac{m\pi}{2H} \right)^2 \right)}$$

For the simulation the outliers are present to a lesser extent.

C. Comparison open-jet and closed test section

Finally the open-jet and closed test section measurements are compared in Figure 20 by applying the propeller steering function and using the virtual source location from the open-jet simulations. It is found that both measurements are similar while the outliers for the experiment are found close to the tunnel modes.

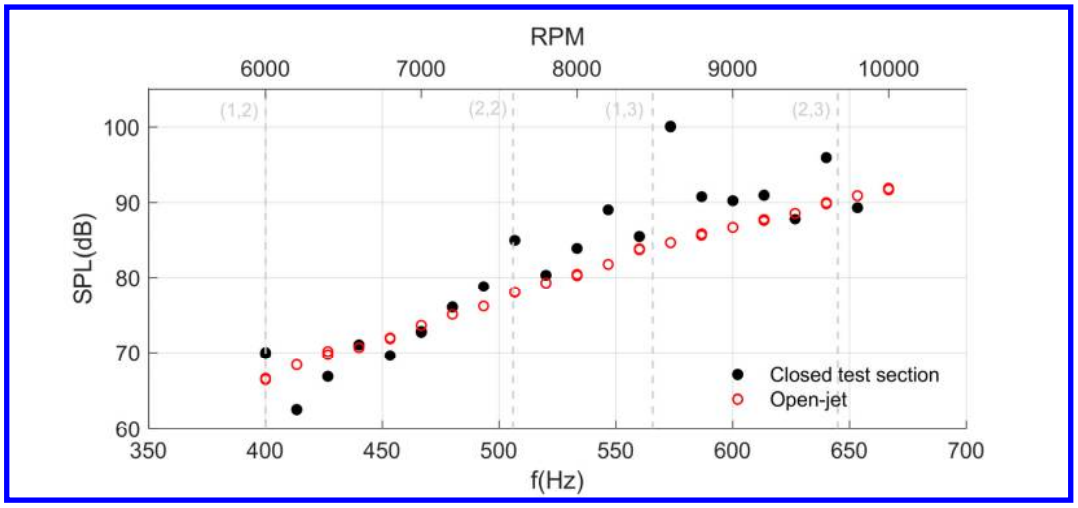

Figure 20: Comparison between experimental measurements in the open-jet and closed test section.

VI. Conclusion

In this paper measurements and simulations of a small propeller are described. The following conclusions can be made:

- Due to the large depth of field for low-frequencies in the near-field it is difficult to determine the virtual source location in experimental conditions. For the open-jet the large depth of field is the main issue while for the closed test-section measurements the influence of reflections are an additional challenge.
- With the introduced propeller steering function the propeller source can be more easily defined. This can especially be of use in measurements where different sources have to be separated such as for example in closed test section measurements where image sources play a role.
- At operating conditions close to resonances in the hard-walled environment imposes extra challenges to determine the source level correctly.

References

[1] J. Marte and D. Kurtz, "A review of aerodynamic noise from propellers, rotors and lift fans," Technical Report 32-1462 NASA, 1970.

[2] P. Sureshkumar, M. Kingan and A. Parry, "Predicting the noise of an open rotor in a wind tunnel," *International Journal of Aeroacoustics,* vol. 18, no. 4-5, pp. 414-443, 2019.

[3] J. Fischer and C. Doolan, "Improving acoustic beamforming maps in a reverberant environment by modifying the cross-correlation matrix," *Journal of Sound and Vibration,* vol. 411, pp. 129-147, 2017.

[4] C. Horvath, E. Evia and G. Podboy, "Limitations of phased array beamforming in open rotor noise source imaging," NASA, Cleveland, 2013.

[5] H. Brouwer, "On the use of the method of matched asymptotic expansions in propeller aerodyanmics and acoustics," *Journal of Fluid Mechanics,* vol. 242, pp. 117-143, 1992.

[6] E. Sarradj, "Three-dimensional acoustic source mapping with different beamforming steering vector formulations," *Advances in acoustics and vibration,* 2012.

[7] N. Peake and W. Boyd, "Approximate method for the prediction of propeller noise near field effects," *Journal of Aircraft,* vol. 30, no. 5, pp. 603-610, 1993.

[8] M. Tuinstra and M. van der Meulen, "Acoustic location by tomographic reconstruction," Delft, 2019.